

Cyclic motion and inversion of surface flow direction in a dense polymer brush under shear

M. MÜLLER¹ ^(a) and C. PASTORINO²

¹ *Institut für Theoretische Physik, Georg-August Universität, Friedrich Hund-Platz 1, 37077 Göttingen, Germany*

² *Dept. de Física, Centro Atómico Constituyentes, CNEA-CONICET, Av. Gral. Paz 1499, 1650 Pcia. de Buenos Aires, Argentina*

PACS 83.50.Lh – Slip boundary effects (interfacial and free surface flows)

PACS 61.25.Hq – Macromolecular and polymer solutions; polymer melts; swelling

PACS 82.20.Wt – Computational modeling; simulation

Abstract. – Using molecular simulations, we study the properties of a polymer brush in contact with an explicit solvent under Couette and Poiseuille flow. The solvent is comprised of chemically identical chains. We present evidence that individual, unentangled chains in the dense brush exhibit cyclic, tumbling motion and non-Gaussian fluctuations of the molecular orientations similar to the behaviour of isolated tethered chains in shear flow. The collective molecular motion gives rise to an inversion of hydrodynamic flow direction in the vicinity of the brush-coated surface. Utilising Couette and Poiseuille flow, we investigate to what extent the effect of a brush-coated surface can be described by a Navier slip condition.

Introduction. – Grafting polymers onto surfaces is a versatile and stable method for controlling wettability, lubrication, adhesion and surface interactions [1]. Brush coatings are utilised for biocompatibilisation or as antifouling coatings in microfluidic devices. They are employed to stabilise colloids or, in form of interfacial layers of copolymers, to prevent coalescence of droplets in polymer blends. ¹ Dense polymer brushes give rise to fascinating dynamical properties like a dramatic reduction of friction between two brushes sliding past each other [2], incompletely understood collective dynamics [3], additional dissipation mechanisms of droplets moving on brushes due to the deformability of the soft elastic surface [4], and large effective slip lengths [5].

Simulations of dense polymer brushes with an *explicit solvent* [6–9] are computationally very demanding and previous studies of brushes in shear flow [10–14] conceived the brush as a porous medium [15] utilising Brinkman’s equation [16] to quantify the penetration of the solvent flow into the brush. They observed that density profiles normal to the surface are not strongly affected by shear flow but the average molecular conformations are tilted towards and stretched along the direction of the flow.

Isolated grafted chains in shear flow already exhibit intriguing dynamics [17–20]: Thermal fluctuations away from the surface expose the non-grafted chain end to a faster flow and lead to an elongation of the chain in the flow direction. The stretched chain rotates back towards the grafting surface and contracts. Related effects have also been reported for the chain ends in swollen brushes under strong shear and they have been attributed to the non-linear elasticity of the macromolecules [14]. One hallmark of this dynamic behaviour of isolated chains are strongly non-Gaussian distribution functions of angular orientations [18, 20]. Explicit hydrodynamic interactions [19, 20] appear not to be crucial for this cyclic tumbling motion.

Using Single-Chain-in-Mean-Field (SCMF) simulations and Molecular Dynamics (MD) simulations of a brush in contact with an explicit solvent of identical chain molecules we demonstrate that the tumbling motion observed for isolated chains persist as one increases the grafting density and that the individual motion of the tethered molecules results in the inversion of the collective flow direction at the surface. The effect of the brush cannot be described by a Navier slip condition [21–23].

^(a)E-mail: mmueller@theorie.physik.uni-goettingen.de

¹Copolymers at interfaces in blends can laterally move, but the ends of grafted chains in a brush are immobile.

Model and simulation technique. – Brush and melt polymers are represented by a bead-spring model

with $N = 32$ segments per molecule. Harmonic bonding forces \mathbf{F}_b with spring constant $3(N-1)k_B T/R_e^2$ act between neighbours along the chain. R_e^2 denotes the mean square end-to-end distance, k_B Boltzmann's constant and T temperature, respectively. Repulsive interactions between segments are catered for by penalising fluctuations of the local density by an energy [24], $\mathcal{H}_{nb} = \frac{\kappa k_B T}{2} \rho_0 \int d^3\mathbf{r} (\phi_b + \phi_m - 1)^2$ where ϕ_b and ϕ_m denote the normalised density of brush and melt, and $\kappa N = 50$ characterises the inverse compressibility. The segment number density, ρ_0 , determines the invariant degree of polymerisation, $\bar{N} = (\rho_0 R_e^3/N)^2 = 128^2$. We study the flow of a polymer melt over a brush in a slit pore of width D_x . The lateral extensions are $L_y = L_z$, and periodic boundary conditions are applied in y and z directions. At $x = 0$ and D_x , there are repulsive, structureless walls ² that repel segments via a potential ³ of the form: $V_w(\Delta x) = \Lambda_w \exp(-\Delta x^2/2\epsilon_w^2)$ with $\Lambda_w N = 66.6k_B T$, $\epsilon_w = 0.15R_e$, and Δx being the distance of a segment from the surface. The first segment of the brush is grafted at $\Delta x_0 = 0.1R_e$. Couette flow is imposed by moving the grafting points of the brush at the top surface at fixed velocity in y -direction; Poiseuille flow is generated by applying an external body force, \mathbf{F}_{ex} , to all segments in y -direction.

In SCMF simulations [25, 26] one considers a large ensemble of explicit chain configurations that independently evolve in an external field. This field mimics the effect of the non-bonded interactions $W(\mathbf{r}) = \delta\mathcal{H}_{nb}/\delta[\rho_0\phi_b(\mathbf{r})] + V_w$. Its gradient gives rise to a force $\mathbf{F}_{nb} = -\nabla W$. Chain segments evolve via Smart Monte Carlo (SMC) moves [27, 28] with trial displacements

$$\Delta\mathbf{r}_{trial} = (\zeta\langle\bar{\mathbf{v}}\rangle + \mathbf{F})\Delta t/\zeta + \xi\sqrt{2k_B T\Delta t/\zeta} \quad (1)$$

$\mathbf{F} = \mathbf{F}_b + \mathbf{F}_{nb} + \mathbf{F}_{ex}$ denotes the forces acting on a segment, ζ is the segmental friction,⁴ and ξ is a Gaussian random number with zero mean and unit variance. We set $\zeta N = 1$.⁵ $\langle\bar{\mathbf{v}}(\mathbf{r})\rangle$ denotes the hydrodynamic velocity field. Chains exhibit Rouse-like dynamics characteristic for unentangled melts [29] and the Weissenberg number is defined as $Wi \equiv \dot{\gamma}\zeta N R_e^2/(3\pi^2 k_B T)$ where $\dot{\gamma}$ denotes the shear rate.

The *fluctuating, external field*, W , is calculated after every time step, and the densities are constructed by assigning the instantaneous particle positions to a three-dimensional grid with linear spacing $\Delta L = R_e/6$ [26]. The hydrodynamic velocity, $\langle\bar{\mathbf{v}}\rangle$, however, represents the *aver-*

age flow field and must not fluctuate. First, we directly calculate an instantaneous velocity, $\mathbf{v}_i = \Delta\mathbf{r}_i/\Delta t$, of segment i from its explicit displacement [30] during a SMC step (in order to retain spatial resolution) and assign it to the grid. Then, we add the instantaneous velocities of all segments, average over a time period, T , and normalise by the local density to obtain the average local velocity $\langle\bar{\mathbf{v}}(\mathbf{r})\rangle$. This procedure ensure that the average force $\langle\bar{\mathbf{F}}\rangle$ vanishes. This time averaging procedure limits the simulation technique to stationary or slowly varying flows. For the density utilised in our simulations a time interval $T \geq 800\zeta R_e^2/(Nk_B T)$ is sufficient to eliminate fluctuations of the velocity field and to yield accurate predictions in equilibrium.

The computational scheme is similar to dynamic self-consistent field techniques [31–33] or self-consistent Brownian dynamics simulations [12, 14, 34]. With the SMC algorithm we systematically approach the Brownian Dynamics limit ($\Delta t \rightarrow 0$). In the present work, we use the time step $\Delta t = 0.08\zeta R_e^2/(Nk_B T)$ which closely mimics Rouse dynamics. The time step is chosen such that the self-diffusion coefficient and the viscosity in the bulk are close to the Rouse limit, $D_R = k_B T/(\zeta N)$ and $\eta_R R_e/(\zeta N\sqrt{\bar{N}}) = 1/36$, respectively. The acceptance rate of SMC moves is about 83%. We have explicitly verified that a ten times smaller time step yields very similar results. Moreover, our simulations capture density fluctuations [26] and, most importantly, we do not approximate the effect of the brush on the solvent flow by that of a porous medium [15, 16] but use an explicit solvent instead.

To validate the dynamic SCMF simulations, we additionally perform MD simulations of a standard bead-spring model [9, 35]. Grafted and melt chains comprise $N = 32$ segments interacting via a purely repulsive Lennard-Jones potential with length and energy scales, σ_{LJ} and ϵ_{LJ} , and cut-off $r_c = \sqrt[6]{2}\sigma_{LJ}$. Neighbouring segments along a chain are bonded together by a Finitely Extensible Non-linear Elastic (FENE) potential. The temperature, $k_B T/\epsilon_{LJ} = 1.68$, is maintained by a DPD thermostat [36]. The MD simulations correspond to a dense brush, $\sigma R_e^2 = 1.5\sqrt{\bar{N}}$, of short chains, $\bar{N} = 6^2$.

Results. — In Fig. 1a we present the density profile across the slit pore for $D_x = 10R_e$ and grafting density $\sigma R_e^2 = \sqrt{\bar{N}}$ for Couette and Poiseuille flow as obtained by dynamic SCMF simulations. At this moderate grafting density there is a broad interface between brush and melt (“wet brush”) and, in agreement with previous studies [14], the profile normal to the surface does not depend on flow for small shear rates. The depletion at the wall stems from the repulsive segment-wall potential.

Measuring the forces, F_y^{graft} , that act on the grafted segments in Couette flow we obtain the shear stress $\sigma_{xy} R_e^3/k_B T = 29.3$ for Couette flow. Alternatively, we can estimate the intramolecular stress of the melt at the centre of the film via the mean-field approximation

²The melt perfectly slips over the bare surface (without brush). At the considered grafting density, however, the velocity at the wall vanishes (microscopic stick, see Figs. 2 and 4). Thus, our results do not depend on the microscopic boundary condition (slip or stick).

³A repulsive V_w impedes the SMC to propose moves that would penetrate the hard walls and be rejected.

⁴The segmental friction, ζ , is not determined by the intermolecular forces like in a MD simulation but it is a parameter of the algorithm.

⁵For Brownian dynamics the equations of motion are invariant under $\zeta \rightarrow \zeta' = \lambda\zeta$ and $t \rightarrow t' = \lambda t$ and we measure time in units of $\zeta N R_e^2/k_B T$

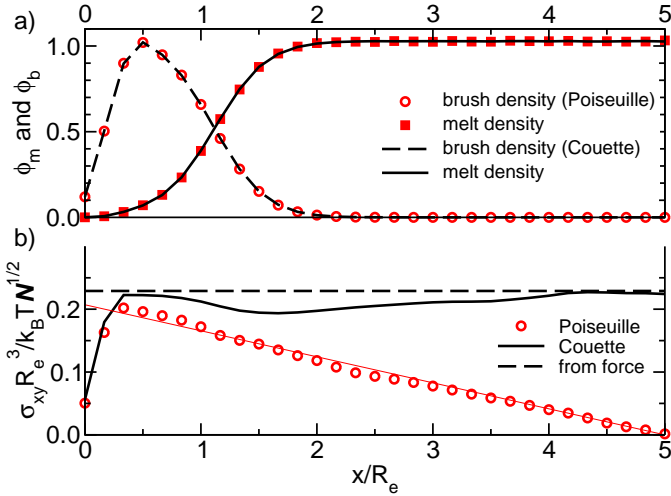


Figure 1: a) Density profiles across a slit of width $D_x = 10R_e$ and lateral extent $L_y = L_z = 4R_e$ for Poiseuille flow ($F_{\text{ex}} N = 0.03k_B T / R_e$, symbols) and Couette flow ($\dot{\gamma}_w \zeta N R_e^2 / k_B T = 5$, $Wi = 0.247$, lines). b) Kramer's stress for Poiseuille and Couette flow. The horizontal dashed line marks the stress obtained from the forces on the grafted ends for Couette flow.

(Kramer's formula [29]⁶) $\sigma_{xy} R_e^3 / (k_B T \sqrt{N}) = (N - 1)(\phi_b + \phi_m) \frac{\langle b_x b_y \rangle}{R_e^2 [3(N - 1)]}$ where b_x and b_y denote the distance between bonded segments perpendicular to the surfaces and along the shear direction, respectively. This estimate is shown in Fig. 1b for Poiseuille and Couette flow. The stress in Couette geometry agrees well with the result obtained from the force on the grafted segments. From the stress at the centre of the film and the velocity gradient (cf. Figs. 2 and 4) we can estimate the dimensionless viscosity, $\eta R_e / (\zeta N \sqrt{N}) = 0.030$ and 0.031 for Poiseuille and Couette flow, respectively.

Fig. 2 presents the velocity across the film for Poiseuille flow. The profile at the centre is parabolic,

$$v_{\text{hydro},y}(x) = \frac{\rho_0 F_{\text{ex}}}{2\eta} (x - x_P)(D_x - x_P - x) \quad (2)$$

as expected from macroscopic hydrodynamics. x_P denotes the position at which this parabolic profile extrapolates to zero. The flow penetrates into the brush [15] and details of the flow in the vicinity of the surface are shown in the panel (a) of Fig. 2. Unexpectedly, the hydrodynamic velocity profile in the vicinity of the grafting surface becomes negative, *i.e.*, the flow direction is *opposite* to the driving force F_{ex} . This inversion of the collective flow direction at the grafting surface is a consequence of the individual motion of grafted chains, *i.e.*, the tumbling motion of grafted chains under shear [14, 17].

To rationalise the observed inversion of flow at the surface, it is important to distinguish between the time-

⁶We utilise the same spatial assignment of the stress as for the density but other schemes [e.g., J. H. Irving and J. G. Kirkwood, *J. Chem. Phys.*, **18** (1950) 817.] that are locally more accurate can be employed.

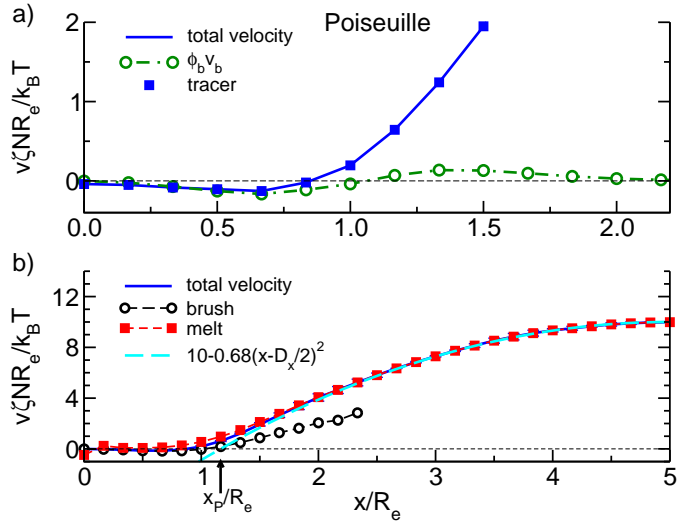


Figure 2: Mass averaged, total velocity profile, $\langle \bar{v}_y \rangle$, and velocity of brush and melt segments for Poiseuille flow. Panel (a) highlights the total velocity at the surface and shows details of $\phi_b v_{b,y}$ for a system that additionally contains 1% tracer particles (*i.e.*, 6554) which have the same extension as a monomeric unit and friction coefficient $\zeta = 1$. Note that the velocity profiles of the tracers coincides with $\langle \bar{v} \rangle$. Panel (b) shows the velocity profiles across half of the film. The dashed line is a fit to macroscopic predictions (cf. Eqs. (2)). The arrow marks the positions, x_P , at which the extrapolation of the macroscopic hydrodynamic velocity profile vanishes.

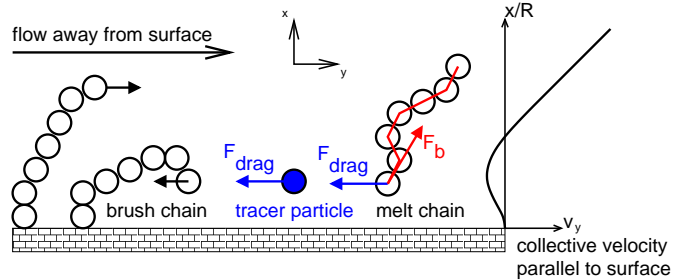


Figure 3: Sketch of the molecular motion of the grafted molecules of the brush, the free chains of the melt and the smaller tracer particles. On the left, brush molecules in two different stages of their tumbling motion are depicted and the velocity of the end-segment is highlighted by an arrow. This graph illustrates that the collective velocity of the brush segments at a specific distance from the surface need not to vanish although the time-averaged velocity of each segment of grafted chains is zero. In the middle, the forces that act on the tracer particle and a segment of a free chain near the surface are illustrated. On the right hand side, the collective, hydrodynamic velocity profile, $\langle \bar{v} \rangle$, of all segments is shown.

averaged velocity of individual segments and the position-dependent, hydrodynamic flow, $\langle \bar{v}(\mathbf{r}) \rangle$. In the steady state, the time-averaged velocity of each individual segment of the grafted chains must vanish because they are irreversibly grafted to the substrate. This property implies $\int dx \phi_b(x) v_{b,y}(x) = 0$, which is obeyed in our simulations

as shown in Fig. 2a. The drag force, exerted by the x -dependent, hydrodynamic flow field, $\langle \bar{v}_y \rangle(x)$, couples the motion in the parallel and perpendicular directions and gives rise to a correlation between the position, x , of a brush segment and its velocity, v_y . A brush segment that is farther away from the grafting surface experiences a larger drag force and has, on average, a larger parallel velocity, $v_{b,y}$, than the same segment when it is located closer to the grafting surface and exposed to a smaller (inverted) drag. This effect is illustrated in Fig. 3. In Fig. 2b, one clearly observes that the very few segments of the brush that extend far into the melt, $x/R_e > 2$, are dragged along with the flow and have a large positive velocity ($v_{b,y}(x) \gtrsim \frac{1}{2}\langle \bar{v}_y \rangle(x)$). Since they are grafted, they must compensate this by a negative velocity when they are closer to the grafting surfaces. This mechanism results in the cyclic motion of the individual molecules. Our simulations show that this cyclic motion is not necessarily a consequence of the non-linear elasticity of the chain molecules [14] and that it also persists in moderately dense brushes. Averaging the velocity of all brush segments in the vicinity of the surface, we obtain a negative velocity and, since the density of the melt chains is low at the surface, the negative velocity inside the brush is sufficient to invert the *total, mass averaged velocity profile* $\langle \bar{v} \rangle$ (cf. Fig. 2a).

For the choice of parameters, the velocity profile of the free chains of the melt does not exhibit an inversion of the flow direction at the surface. Since the free chains only weakly penetrate the brush, the larger part of the extended molecule is exposed to flow in the positive direction at the centre even if a single segment is located close to the surface. In this case, the drag force on this near-surface segment is compensated by the bonding force (as sketched in the middle of Fig. 3) and no inversion of the flow is observed. To observe the inversion of the flow direction of freely moving particles at the surface, we have added 1% of monomeric tracer particles (i.e., 6554 beads), which have identical size than the polymer segments and friction coefficient, $\zeta = 1$. In Fig. 2a, we demonstrate that the velocity profile of these free tracer particles exhibits flow inversion at the surface and that such particles potentially can be used to experimentally detect the inversion of the flow direction at the surface.

We expect that the inversion of the velocity is characteristic for intermediate grafting densities. At very small grafting densities, the flow at the surface is dominated by the velocity of the solvent and the cyclic motion of the grafted chains will not be sufficient to invert $\langle \bar{v} \rangle$. Contrary, if the brush was strongly stretched, the width of the brush-melt interface would be narrow, the height fluctuations of brush segments would be small and – in the Lennard-Jones model and experiments – topological constraints would become more important. These effects would shift the inversion zone away from the grafting surface and tend to reduce the inversion of the flow.

To verify that the inversion of velocity profile at the

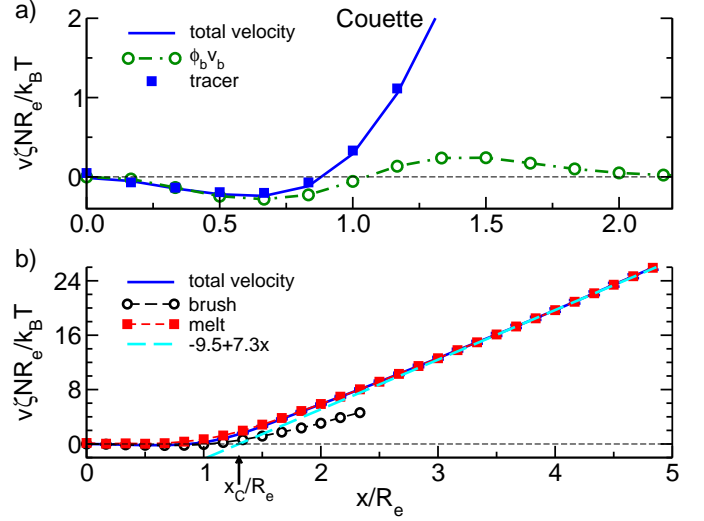


Figure 4: Mass averaged, total velocity profile, $\langle \bar{v}_y \rangle$, and velocity of brush and melt segments for Couette flow. Panel (a) highlights the total velocity at the surface and shows details of $\phi_b v_{b,y}$ for a system that additionally contains 1% tracer particles (cf. Fig. 2). Panel (b) shows the velocity profiles across half of the film. The dashed line is a fit to macroscopic predictions (cf. Eqs. (3)). The arrow marks the positions, x_C , at which the extrapolation of the macroscopic hydrodynamic velocity profile vanishes.

brush-coated surface is independent from the way the flow is generated we have studied Couette flow, moving the grafted chain ends at the top surface with constant velocity $\dot{\gamma}_w D_x$. The velocity profile across the pore is shown in Fig. 4.⁷ The linear behaviour at the centre corresponds to macroscopic hydrodynamics

$$v_{\text{hydro},y}(x) = \dot{\gamma}(x - x_C) \quad (3)$$

but at the surface the flow direction is inverted. x_C denotes the location where this macroscopic linear velocity profile vanishes. If we used this as the definition of an effective slip length, the slip length would be negative [9].

To validate this observation, we additionally perform MD simulations of a standard Lennard-Jones bead-spring model. Fig. 5a presents the density profiles of brush and melt segments while panel b presents the total velocity profiles for Poiseuille and Couette flow. The inversion of the flow direction inside the brush is confirmed. Importantly, the MD simulations do not invoke any approximation: They do not ignore inertia effects and do not replace intermolecular interactions by quasi-instantaneous external fields [26]. They capture the local packing of a dense polymeric fluid (see density oscillations in Fig. 5a), the finite extensibility of bonds and, importantly, the non-crossability of the chain molecules.

⁷Only the bottom half of the slit is shown in Fig. 4 Due to Galilean invariance, the flow velocity at the top wall is positive and segments at the top wall move in the positive direction with a higher velocity than the top wall.

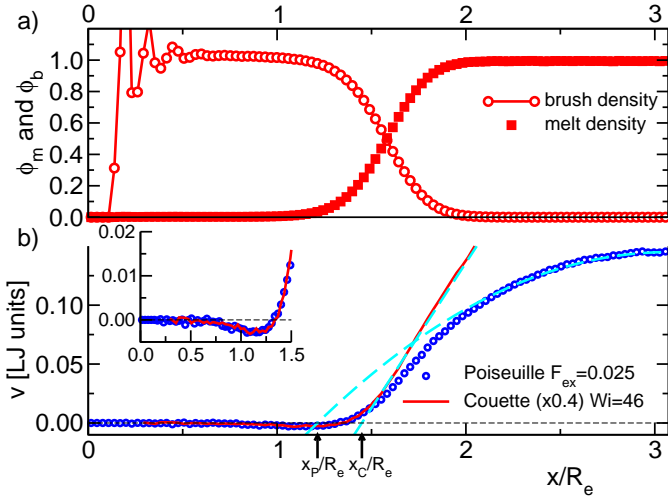


Figure 5: a) Density profile of the brush-melt interface obtained from the MD simulations using a bead-spring model ($N = 32, R_e = 6.51\sigma_{LJ}, \sigma R_e^2 = 8.9, \rho_0\sigma_{LJ}^3 = 0.69, \sqrt{N} = 5.95, k_B T/\epsilon_{LJ} = 1.68$). b) Mass averaged velocity profile $\langle v_y \rangle$ for Poiseuille flow with $F_{ex}\sigma_{LJ} = 0.025\epsilon_{LJ}$ and Couette flow with $Wi = 46$. The data for Couette flow have been scaled by a factor 0.4. The arrows mark x_P and x_C . The inset highlights the velocity at the surface.

Utilising the simulation results of Poiseuille and Couette flow we try to extract the parameters of the hydrodynamic boundary condition [23] that serves to match the detailed microscopic velocity profile in the vicinity of the brush-coated surface with macroscopic hydrodynamics, \mathbf{v}_{hydro} . The Navier slip condition [21] assumes that the viscous stress $\sigma_{xy}^{visc} = \eta \frac{dv_{hydro,y}}{dx}$ calculated from the macroscopic hydrodynamic velocity profile, \mathbf{v}_{hydro} , equals the friction stress $\sigma_{xy}^{fric} = \frac{\eta}{\delta_b} v_{hydro,y}$ at a distance, x_b . δ_b denotes the slip length and x_b the effective position of the hydrodynamic boundary. Both parameters are assumed to be materials properties that characterise the coated surface independently from the strength and type of flow. From Eqs. (2) and (3) one obtains $\delta_b = \sqrt{(x_P - x_C)(D - x_C - x_P)}$ and $x_b = x_C + \delta_b$. Thus, a necessary condition for simultaneously describing both types of flows by the same parameters, x_b and δ_b , is $x_P \geq x_C$ which is neither fulfilled by the profiles extracted from the SCMF simulations with $D_x = 10R_e$ (see Figs. 2 and 4) nor by those obtained from MD simulations of the bead-spring model with $D_x = 6.14R_e$ (cf. Fig. 5).

Finally, in Fig. 6 we analyse the fluctuations of the angle, φ , between the projection of the chain's end-to-end vector on the grafting surface and the flow direction (see inset) for different shear rates. Similar to the behaviour of isolated chains [18, 20], the wings of the distribution for moderate Weissenberg numbers are compatible with $P(\varphi) \sim 1/\sin^2 \varphi$. This non-Gaussianity of the distribution is corroborated by the MD results. At comparable Weissenberg number, the effect is smaller for the Lennard-Jones brush because of the higher grafting den-

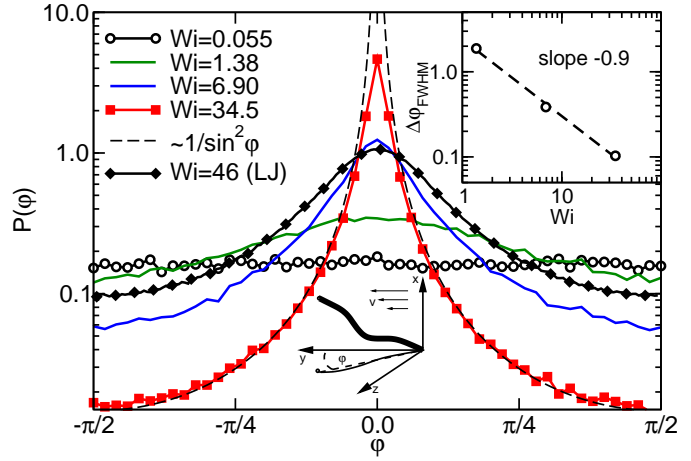


Figure 6: Probability distribution of the angle, φ (see lower sketch). For moderate shear, the distribution is sharply peaked around $\varphi = 0$ and its wings are compatible with $P(\varphi) \sim 1/\sin^2(\varphi)$ (dashed line). SCMF simulation data are obtained for $D_x = 6R_e$ and $L_y = L_z = 2R_e$. The time step Δt for the highest shear rate, $Wi = 34.5$, has been decreased by a factor 0.1. The MD simulation data of the bead-spring model with $Wi = 46$ are presented by filled symbols. The upper inset presents the width of the distribution as a function of the Weissenberg number.

sity and non-crossability. The full width at half maximum $\Delta\varphi_{FWHM}$ of the distribution is compatible with $\varphi_{FWHM} \sim Wi^{-0.9}$ in agreement the corresponding predictions for isolated chains and low shear rates.

Conclusion. — In summary, dynamic SCMF and MD simulations of polymer brushes in an explicit solvent show that the motion of chains in a dense brush is similar to the cyclic tumbling of isolated grafted chain in shear flow [17]. We find that brush chains are not uniformly tilted by the flow but the orientation of the molecular axis with the flow direction is characterised by a non-Gaussian distribution [18, 20]. The individual tumbling motion of the brush molecules leads to an inversion of the total, collective flow velocity at the grafting surface. It would be interesting to quantitatively compare simulations with an implicit solvent using Brinkman's equation and our simulations with an explicit solvent to assess to what extent the brush can be described as a static porous medium. The simulation also provide microscopic insights into the mechanisms that dictate the hydrodynamic boundary condition. The latter is important for controlling flow in microfluidic devices. The cyclic tumbling motion of the individual brush molecules could also potentially serve to separate particles with different surface affinities by flow or to promote mixing close to the grafting surface.

We thank M.P. Allen, K.Ch. Daoulas, G.H. Fredrickson, A. Milchev, S. Minko, and C. Servantie for inspiring dis-

cussions. Financial support was provided by the priority program “Nano- and Microfluidics” MU1674/3-2, the IN-FLUS project, the DAAD/SECYT, and ANPCYT (PME 2003, PICT 2005). Computing time at NIC Jülich, HLRN Hannover, and GWDG is acknowledged.

References

- [1] ZHAO B. and BRITTAIN W. J., *Prog. Polym. Sci.*, **25** (2000) 677.
- [2] KLEIN J., KUMACHEVA E., MAHALU D., PERAHIA D., and FETTERS L. J., *Nature*, **370** (1994) 634.
- [3] YAKUBOV G. E., LOPPINET B., ZHANG H., RUHE J., SIGEL R., and FYTAS G., *Phys. Rev. Lett.*, **92** (2004) 115501.
- [4] CARRE A., GASTEL J. C., and SHANAHAN M. E. R., *Nature*, **379** (1996) 432.
- [5] FETZER R., JACOBS K., MUNCH A., WAGNER B., and WITELSKI T. P., *Phys. Rev. Lett.*, **95** (2005) 127801.
- [6] PETERS G. H. and TILDESLEY D. J., *Phys. Rev. E*, **52** (1995) 1882.
- [7] GREEST G. S., *J. Chem. Phys.*, **105** (1996) 5532.
- [8] GREEST G. S., *Adv. Polym. Sci.*, **138** (1999) 150.
- [9] PASTORINO C., BINDER K., KREER T., and MÜLLER M., *J. Chem. Phys.*, **124** (2006) 064902.
- [10] LAI P. Y. and BINDER K., *J. Chem. Phys.*, **98** (1993) 2366.
- [11] MIAO L., GUO H., and ZUCKERMANN M. J., *Macromolecules*, **29** (1996) 2289.
- [12] DOYLE P. S., SHAQFEH E. S. G., and GAST A. P., *Phys. Rev. Lett.*, **78** (1997) 1182.
- [13] DOYLE P. S., SHAQFEH E. S. G., and GAST A. P., *Macromolecules*, **31** (1998) 5474.
- [14] SAPHIANNIKOVA M. G., PRYAMITSYN V. A., and COS-GROVE T., *Macromolecules*, **31** (1998) 6662.
- [15] MILNER S. T., *Macromolecules*, **24** (1991) 3704.
- [16] BRINKMAN H. C., *Applied Scientific Research Section A-Mechanics Heat Chemical*, **1** (1947) 27.
- [17] DOYLE P. S., LADOUX B., and VIOVY J. L., *Phys. Rev. Lett.*, **84** (2000) 4769.
- [18] GERASHCHENKO S. and STEINBERG V., *Phys. Rev. Lett.*, **96** (2006) 038304.
- [19] DELGADO-BUSCALIONI R., *Phys. Rev. Lett.*, **96** (2006) 088303.
- [20] WINKLER R. G., *Phys. Rev. Lett.*, **97** (2006) 128301.
- [21] NAVIER C. L. M. H., *Mem. Roy. Sci. Inst. France*, **6** (1823) 389.
- [22] WOLYNES P. G., *Phys. Rev. A*, **13** (1976) 1235.
- [23] BOCQUET L. and BARRAT J. L., *Phys. Rev. Lett.*, **70** (1993) 2726.
- [24] HELFAND E. and TAGAMI Y., *J. Chem. Phys.*, **56** (1972) 3592.
- [25] MÜLLER M. and SMITH G. D., *J. Polym. Sci. B: Polymer Physics*, **43** (2005) 934.
- [26] DAOULAS K. C. and MÜLLER M., *J. Chem. Phys.*, **125** (2006) 184904.
- [27] ROSSKY P. J., DOLL J. D., and FRIEDMAN H. L., *J. Chem. Phys.*, **69** (1978) 4628.
- [28] ALLEN M. and TILDESLEY D., *Computer Simulation of Liquids*. Clarendon Press, Oxford (1987).
- [29] DOI M. and EDWARDS S., *The Theory of Polymer Dynamics*. Oxford University Press, New York (1994).
- [30] NARAYANAN B. and GANESAN V., *Phys. Fluids*, **18** (2006) 042109.
- [31] FRAAIJE J. G. E. M., *J. Chem. Phys.*, **99** (1993) 9202.
- [32] MORITA H., KAWAKATSU T., and DOI M., *Macromolecules*, **34** (2001) 8777.
- [33] LO T. S., MIHAJLOVIC M., SHNIDMAN Y., LI W. T., and GERSAPPE D., *Phys. Rev. E*, **72** (2005) 040801.
- [34] NARAYANAN B., PRYAMITSYN V. A., and GANESAN V., *Macromolecules*, **37** (2004) 10180.
- [35] KREMER K. and GREEST G. S., *J. Chem. Phys.*, **92** (1990) 5057.
- [36] PASTORINO C., KREER T., MÜLLER M., and BINDER K., *Phys. Rev. E*, **76** (2007) 026706.